Article

A Database of Computation-Ready 2D Zeolitic Slabs

Omar Knio, Andrew J. Medford, Sankar Nair, and David S. Sholl

A Database of Computation-Ready 2D Zeolitic Slabs

Omar Knio, Andrew J. Medford, Sankar Nair, and David S. Sholl*

School of Chemical & Biomolecular Engineering, Georgia Institute of Technology, 311 Ferst Drive NW, Atlanta, GA 30332-0100, United States

ABSTRACT: Zeolites are nanoporous aluminosilicates widely used in catalysis and separations applications. Though generally formed as 3D crystals, new synthesis techniques have given access to 2D zeolite nanosheets with small diffusion path lengths and accelerated molecular diffusion. Since most previous research has focused on bulk zeolite crystals, there is little understanding of the surface adsorption and diffusion mechanisms likely involved at such length scales and their contributions to the permeability and selectivity of different species. To enable the systematic examination of such surface properties, we constructed a database of more than 800,000 computation-ready 2D zeolite nanosheets from the full range of known zeolite structures in the IZA database of zeolite structure types. The nanosheet surfaces cover a wide range of orientations and were created *via* the principle of minimizing the number of bonds broken during the termination of a unit cell. The database consists of two sets of nanosheets: one set with known heights and unrelaxed surfaces, and another set with arbitrary heights and relaxed surfaces. As an initial example of the utility of this database, we generated equilibrium Wulff shapes for 203 3D zeolite structure types in the International Zeolite Association (IZA) database.

INTRODUCTION

Nanoporous materials such as zeolites are of great interest as adsorbents, catalysts, and membranes in a number of chemical production applications. For example, membrane separations can be up to 90% more energy efficient than distillation.[1] However, zeolitic membranes have generally faced difficulties in scale-up of expensive steps and materials degradation[2], and their current industrial application is focused upon dehydration of organic-water mixtures.[3, 4] New synthesis techniques have led to the synthesis of 2D zeolite nanosheets wherein crystallization is restricted to two dimensions and the third is only a few unit cells in thickness.[5-7] This confers a number of attractive properties such as lower diffusion resistance (especially for large molecules), very high surface areas, and direct surface access to shape/size-selective catalytic sites that would otherwise be embedded inside a 3D zeolite crystal. Although it is known that diffusion is enhanced in nanosheets relative to bulk materials, the dominant surface diffusion and blockage mechanisms and their magnitude with respect to bulk diffusion, remain largely unknown.[8-13] It has been suggested that surface diffusion through nanosheets can be retarded by repeated cycles of entry and exit into the silica layers.[13] Other proposed mechanisms for diffusion in zeolitic nanosheets involve pore blockage by adsorption of water on silanol groups, pore narrowing, and high rates of desorption from the surface.[11, 14] Separate studies have reported enhanced water permeability as a result of increasing zeolite surface hydrophilicity.[8, 15]

A significant challenge to systematically examining these issues is that very limited structural information is available on 2D zeolitic nanosheets. Zeolite databases with bulk (3D) material structures have been generated by a variety of methods. The International Zeolite Association (IZA) database contains more than 200 experimentally known zeolites.[16, 17] To expand upon the properties of synthesized zeolites, several computational groups have created databases of hypothetical zeolite frameworks.[18] Foster and Treacy developed the symmetry constrained intersite bond searching (SCIBS) method and obtained a database of over 2 million structures.[19, 20] Their database contained 97 IZA frameworks, and two predicted 18-membered ring pore frameworks were later synthesized as ITQ-33 and ITQ-44.[18, 21, 22] Friedrichs et al. systematically enumerated the structural possibilities of networks of 4-connected atoms and matched predicted tilings to known IZA structures.[23] Yu and Xu developed hypothetical structures by placing atoms around forbidden zones to achieve the desired porous pattern.[18] Pophale, Cheeseman, and Deem developed a database of hypothetical zeolites using a Monte Carlo search for zeolite like materials.[24] About 15% of the structures had energy densities within the range occupied by known zeolites.[24]

As mentioned earlier, the above databases listed only describe bulk (3D) zeolite materials. To accelerate the development of 2D zeolitic nanosheets, it would be useful to have access to a wide range of 2D zeolite structures. To that end, Jamali et al. developed a database of 27 zeolite nanosheets and screened the structures for potential use in water desalination.[25] Their work identified the four most promising nanosheets based on their pore limiting diameter and channel density properties.[25] Witman et al. recently systematically enumerated minimum bond cut surface terminations and developed a descriptor based on the favorability of the two most favorable Miller indices to

determine the potential of synthesizing a nanosheet from a particular zeolite framework .[26] Their results provided structures for 3,682 surfaces representing 91% of the bulk structure types in the IZA database. In this paper, we describe a different approach that leads to a set of 804,842 structures that exceed in their quantity, span of heights, and surface diversity the nanosheets of any previous work.[25, 26] Our database includes the different surfaces/nanosheets that result from multiple possible terminations of a zeolite surface at a given Miller plane, and includes nanosheet slabs of arbitrary thickness along all crystallographic planes for which the absolute value of each Miller index is < 3. We have generated an average of 705 different surface terminations for about 92% of the bulk structures in the IZA database. As an initial application for our collection of structures, we discuss the equilibrium Wulff shapes predicted for 86% of the IZA structures.

ZEOLITE SURFACE GENERATION

Throughout this paper, we consider zeolitic surfaces of siliceous materials that can be defined as Miller index surfaces of known bulk zeolite structures. It is not obvious *a priori* which Miller indices are most relevant for a given bulk structure. One way to get insight into this issue is to list the Miller indices of surfaces that have been observed experimentally on various zeolite crystals. A partial list is given in **Table S1** (Supporting Information), which includes examples such as the {211} surface of ANA and the {-202} surface of LAU.[27] This list indicates that a range of Miller indices must be considered in any effort to define surface structures for a diverse collection of zeolites. We define the Maximum Miller index (MMI) as the maximum of the absolute values of each index in the set *{hkl}*.[9] The results in Table S1 show that 97% of the observed Miller indices have an MMI < 3. In addition, the number of unique Miller index surfaces that must be considered increases rapidly as MMI is increased. For example, MFI has 19 unique Miller index surfaces with MMI = 2 and 49 unique surfaces with MMI = 3. Moreover, the number and complexity of candidate structures that must be considered for each Miller index typically increases as MMI increases. We therefore used an MMI of 2 in our calculations, and we set out to examine every Miller index surface satisfying this restriction for each bulk structure. We applied our methods to 217 of the 221 tetrahedrally coordinated (non-interrupted) framework materials as defined by the IZA database; four were excluded due to memory requirements.[16] The IZA database includes an additional 14 structures that are not fully tetrahedrally coordinated and denoted with a "-" sign before the framework (for example, structure type "-CLO").[16] These structures were excluded from our analysis.

A goal of our work is to generate structures with the atomic accuracy necessary for geometric calculations and diffusion property analysis.[10, 28-31] With this in mind, we note that the atomic coordinates from the IZA database are only estimates of a pure silica unit cell.[16, 17] To refine the IZA bulk structures, each bulk unit cell was relaxed with the ReaxFF force field using the LAMMPS Molecular

Dynamics package.[32, 33] This force field was chosen because it allows for the effective relaxation of complex surface terminations and is parameterized to accurately account for bond breaking and formation events necessary for surface energy calculations.[32, 34] Each cell was relaxed for 40 loops of conjugate gradient descent energy minimization with an energy tolerance of 10^{-8} and a force tolerance of 10^{-10} kcal/mole-Å. The effect of relaxation on several cells is shown in **Table S2**. All calculations generating surfaces started with bulk unit cells that had been optimized as just described. Generation of surfaces with arbitrary Miller indices was then accomplished with the Pymatgen software package.[35] Pymatgen was first used to reduce the full set of {*hkl*} Miller indices to a minimal set of symmetry-equivalent (*hkl*) Miller indices using the space group symmetry of the bulk material.[35] For each (*hkl*) index of this kind, a Lattice Reoriented Unit Cell (LRUC) was then generated such that the original Miller index of interest is oriented along the *c* axis of the LRUC.[35] In principle, any termination of a material perpendicular to the *c* axis of an LRUC defines an (*hkl*) surface of the material. However, termination of zeolite surfaces requires breaking of chemical bonds, so appropriate choices must be made regarding the location of these terminations to generate chemically meaningful surfaces. The general principle adopted is that surfaces should be terminated to minimize the number of broken bonds relative to other possible terminations.[26] In all cases we assume that broken bonds are -OH terminated in the final slab.
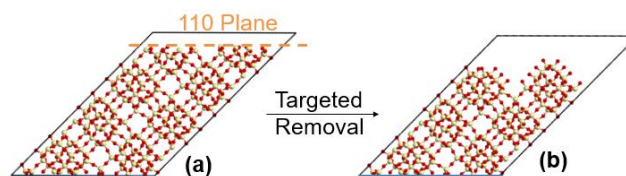
Figure 1. (a) A primary surface of the MFI (110) LRUC. (b) A surface obtained after several targeted corrections with only Q³ Si on the surface. The blue line at the bottom of the LRUC represents a boundary with the bulk structure.

Surfaces were generated from LRUCs in two phases: primary surface generation and targeted removal. In primary surface generation, a plane parallel to the reoriented surface is placed at a Si atom, and all Si atoms above this plane are removed. **Fig. 1a** shows one of the many possible examples of a primary surface for the (110) LRUC of MFI. This process was repeated for every Si with unique coordinates along the *c* axis in the LRUC. For the (110) direction in MFI, this process generates 96 different primary surface terminations.

Each round of targeted removal proceeds in three steps. In step 1, the number of bonds connecting to each Si on the surface is counted, and the Si is labeled as Q^n, where n is the number of Si connected to the labeled Si via an O atom. In step 2, all Q^2, Q^1, and Q^0 Si are removed from a candidate surface structure with the aim of finding a surface structure containing only Q³ Si. An all Q³ surface was chosen as a target because Q³ atoms have the least number of broken bonds and would therefore be expected to

minimize the number of broken bonds on the surface. The removal of Q^2 Si breaks two bonds, and gets rid of two broken bonds, so its effect on the total number of broken bonds on a surface is neutral. The removal of a Q^1 atom breaks one bond and removes three broken bonds. Therefore, in step 3, all Q^1 and Q^0 Si are removed to increase the number and diversity of surfaces that fall within the minimum bond broken tolerance. At the completion of step 3, the surface is saved as a potential surface and sent to another round of targeted removal. The removal of $Q^{<3}$ Si can sometimes convert a Q^3 Si to $Q^{<3}$ Si, so the procedure is repeated 9 times for each primary surface, generating a total of 10 surfaces. The process terminates once an all Q^3 surface is found but does not continue past 9 iterations. **Fig. 1b** shows an example of an MFI (110) surface generated in this way. On MFI (110), the 96 primary surfaces resulted in 193 corrected surfaces (not 960 since many were identical), and 55% of primary surfaces terminated in an all Q^3 surface after an average of 3.6 removal steps. An analysis in the Supporting Information shows that 9 iterations were sufficient to find at least 1 all Q^3 surface for each MFI Miller index examined.

Our algorithm finds the minimum number of broken bonds by heuristically relying on the number of surfaces generated. A comparison of our method to that of Witman et al. shows that our method succeeds in finding the minimum number of broken bonds in almost all instances.[26] Specifically, out of the 108 Miller indices used to create the 8 Wulff constructions in Figs 9-10, only one Miller index, MER (212), did not possess the minimum number of broken bonds. For this specific surface, our algorithm found 22 broken bonds to be the minimum while Witman et al. found 20 broken bonds to be the minimum.[26] We view a success rate of finding the minimum bond count of more than 99% to be adequate for the creation of our database.

Fig. 2 illustrates the formation of a surface that can terminate the upper part of a slab. In a nanosheet, the lower part of a slab will also require a surface termination, so primary surfaces are generated in an identical manner with atoms being removed below the plane instead of above. Targeted removal is then used to refine the surface in the same way described previously. The end result is a set of lower surfaces that can terminate the bottom end of a slab. For MFI (110), the 96 primary surfaces produced 180 such corrected surfaces.
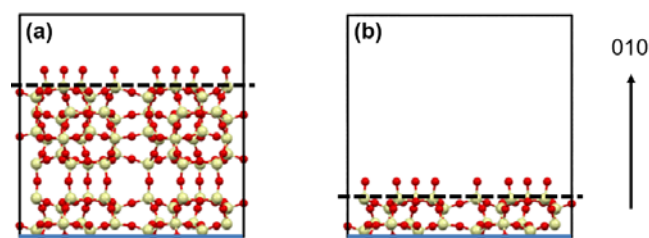
Figure 2. Two MFI (010) surface cells showing surfaces from the same surface symmetry family at fractional coordinates of (a) 0.17 and (b) 0.67 along the *b* axis. The dashed line represents the average surface Si positions and the blue line represents the boundary with the bulk structure.

After surface generation, surfaces were analyzed to determine their total broken bond count. For each Miller index of a specific bulk structure, the number of broken bonds on all surfaces was counted and the minimum noted. Only surfaces within 130% of the minimum number of broken bonds for each Miller index were retained for further use. The tolerance of 130% was chosen because the surfaces with the lowest broken bond count are not always those with the lowest surface energy (**Fig. S1**). For MFI (110), this procedure generated 57 upper surfaces and 48 lower surfaces. Among the set of surfaces just described, the surface Si (Q^3 or Q^m Si) on some surfaces exhibited symmetry relationships to the surface Si on other surfaces. This is not surprising given the symmetry operations that define the atomic coordinates in zeolite unit cells. For example, in the MFI unit cell, the Si atoms at fractional coordinates of 0.67 along the *b* axis are related to the Si atoms at 0.17 along the *b* axis by a glide plane (**Fig. S2**). Upon the formation of MFI (010) surfaces, two surfaces appear related by this symmetry. Identifying symmetry-related surfaces has several advantages. Most obviously, the total number of distinct surfaces can be reduced. A subtler advantage is that slabs can be generated with symmetry-related top and bottom surfaces, which simplifies the interpretation of surface energies. We return to this point later. A radial distribution function (RDF) was used to develop a fingerprint for each upper and lower surface (**Fig. S3**). Surfaces with the same fingerprint were grouped into a surface symmetry family. For MFI (110), the result was 28 lower surface families with an average of 1.7 members, and 37 upper surface families with an average of 1.5 members. In addition, 28 of the upper surface symmetry families were matched with each of the lower surface symmetry families. Grouping by surface symmetry family allowed generation of unique slabs with identical upper and lower surfaces.

SLAB GENERATION

The methods above generated zeolitic surfaces, but additional operations are needed to form 2D nanosheets. Specifically, an "upper" and "lower" surface must be combined with the appropriate connecting structure to generate a complete 2D sheet, or slab. This process varies depending on the slab height and is illustrated schematically in **Fig. 3**. For a one-unit-cell slab, the upper and lower surface cells are combined such that an atom missing in either surface cell is also missing in the final slab, as shown in **Fig. 3a**. For a two-unit-cell slab, the upper and lower surface cells are joined together as shown in **Fig. 3b**. Slabs of height *n* > 2 unit cells are assembled by adding *n*-2 bulk LRUCs between the upper and lower surfaces; **Figure 3(c)** shows an example of adding 1 LRUC to form a 3 unit cell slab. Because all the structures used in these operations were derived from optimized bulk unit cell structures, no artificial stresses due to structural mismatches occur at boundaries inside the nanosheets. After the formation of each slab, H atoms were added 0.9 Å above the surface O to form chemically stable surface terminations as shown in **Fig. 3d-3e**.[37]

The goal of the database is to facilitate simulations with both thin and thick structures. Structures with thickness
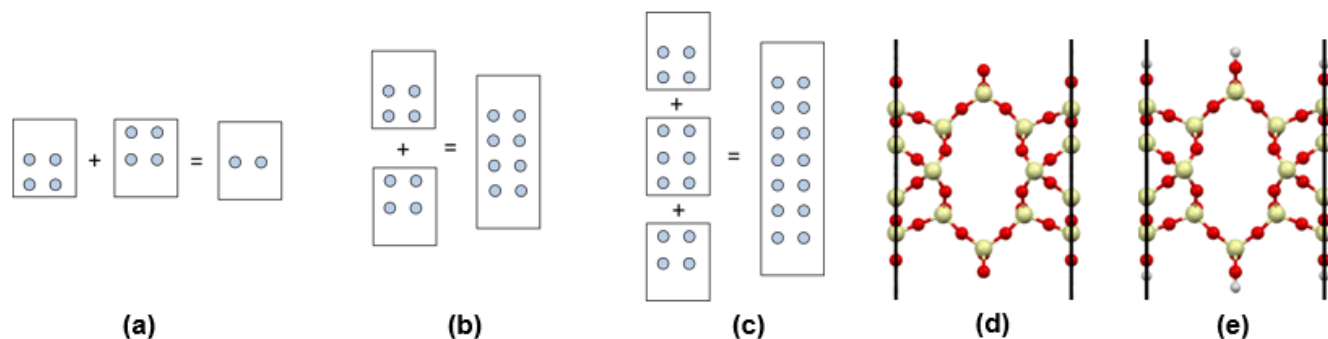
Figure 3. (a) A one unit cell slab formed from an LRUC by the elimination of atoms that are not present in either the upper or lower unit cell. (b) A two unit cell slab formed by the combination of an upper and a lower unit cell. (c) A three unit cell slab formed by the combination of an upper unit cell, an LRUC bulk, and a lower unit cell. (d) A one unit cell EZT (001) slab after formation from an upper and a lower surface. (e) The EZT (001) slab after capping the unbonded O with H to form silanol groups.

es in the nm range, such as nanosheets synthesized with modified structure-directing agents,[5] are easier to directly simulate than larger, micron sized structures, such as 3D crystal cross-sections. In addition to defining the thickness of a zeolitic slab in a simulation, a choice must be made in such simulations between using a flexible or rigid framework. Using a flexible framework uses more computational resources, but in cases where adsorbates are similar in size to the zeolite's pores, flexibility may be crucial in quantitatively predicting molecular diffusivities.[38, 39] These observations suggest it would be helpful to have the option of using rigid frameworks to simulate thicker slabs but that this option would be less necessary in thinner nanosheets. Motivated by this reasoning, two distinct workflows were employed to create two separate databases. The methods described in section 2 generated a comprehensive set of surface terminations, with surfaces related by symmetry operations identified as symmetry families. Starting with each surface symmetry family, the first workflow created a database of nanosheets with a set height and unrelaxed surfaces, while the second workflow created a database of slabs with arbitrary heights and relaxed surfaces as shown in **Fig. 4**. In the first workflow, slabs were formed separately as 1, 2, and 3 unit cell structures as shown in **Fig. 3**. For each slab thickness, an initial set of slabs was formed by a combinatorial matching of all upper surfaces with all lower surfaces from the same surface symmetry family. The initial set of slabs was reduced so each slab was unique as illustrated in **Fig. 5**. In **Fig. 5b**, the slabs u(1/4)-l(3/4) and u(3/4)-l(1/4) are unique while u(3/4)-l(3/4) and u(1/4)-l(1/4) are identical, so only one of the latter two slabs is retained in the database. Some slabs with very small heights were excluded from the database because they were composed of disconnected clusters of atoms. An example is shown in **Fig. S4**. This workflow produced a database of unique slabs with unrelaxed surfaces that had heights of 1, 2, and 3 unit cells.

The second workflow created slab terminations with relaxed surfaces that can be assembled into a slab of any height. This occurred in three phases: assembly, relaxation, and disassembly, as illustrated in **Fig. 6**. During assembly, the upper and lower surfaces are combined with 2 or more LRUCs to form a slab with 4 or more unit cells as shown in **Fig. 6b**. The outer layers of the slab (**Fig. S5**)
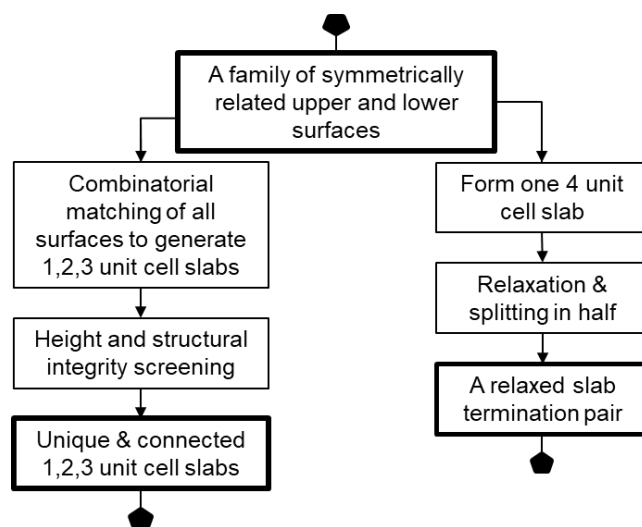
Figure 4. Schematic illustration of methods used to generate a database of thin zeolitic slabs of specified thicknesses (left) and nanosheets that can be used to generate slabs of arbitrary thicknesses (right).
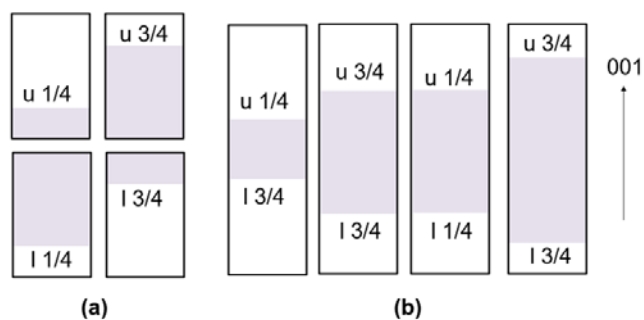
Figure 5. (a) A set of upper and lower surfaces belonging to the same surface symmetry family. Upper surfaces are denoted by a "u(x)", and lower surfaces are denoted by an "l(x)" where x is the fractional coordinate of surface on the c axis of the unit cell. (b) A family of two unit cell slabs formed from the surfaces. Note that there are only three unique slabs because the middle two are identical in height and surface.

were then relaxed with LAMMPS using the ReaxFF force field with one loop of conjugate gradient descent energy minimization with an energy tolerance of 10-8, a force tolerance of 10-10 kcal/mole-Å, and fixed cell parameters.[32, 33] We attempted to use simulated annealing before

conjugate gradient descent to better explore energy space, but that strategy was discarded because in some instances it caused the breakup of the structure at the surface (**Fig. S6**). During relaxation with the Reaxff force field, about 1.4% of surfaces incurred reactions that separated the H from the silanol group or the OH group from the Si. Such surfaces were discarded so that all generated surfaces could be described by force fields that assume tetrahedrally coordinated Si atoms terminated with complete silanol groups.[40-42] An additional 1.9% were rejected due to memory requirements or similar computational errors. After relaxation, the slab was split into a top and bottom slab termination pair as shown in **Fig. 6c**. The two sections can be added to LRUCs to form a slab of any height. The relaxed surfaces often display hydrogen bonding between the H of one silanol group and the O of a neighboring silanol group,[43] so they are representative of real surfaces which are known to exhibit such bonding.[44] An example is shown in **Figures 6d-6e**.
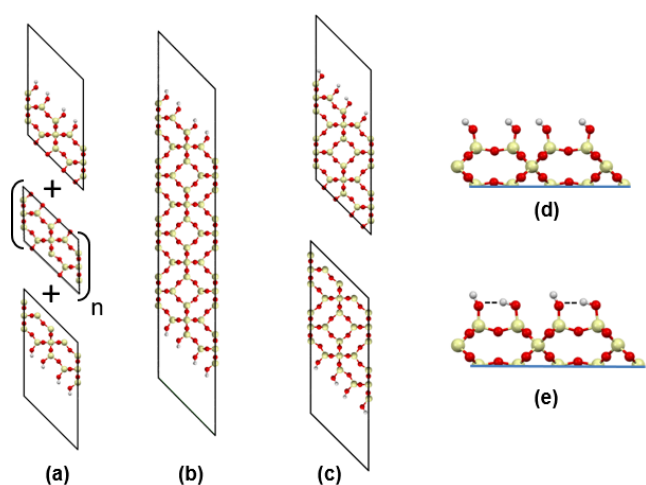
Figure 6. (a) The upper and lower surface unit cells of an SOD (110) symmetry family are combined with *n* LRUCs to form a slab with an identical top and bottom surface. (b) The resulting slab is relaxed with molecular dynamics and split into the (c) top and bottom slab termination pairs. (d) The surface of SOD (110) before relaxation shows the H atoms in their initial position. (e) After relaxation, H bonds (dashed lines) are observed between the H of one silanol group and the O of another silanol group. The blue line at the bottom of (d) and (e) represents a boundary with the bulk structure.

The final slab database contains 3,694 LRUCs, 152,992 slab termination pairs, and 651,850 slabs. A zipped file containing all structures and other documentation is available for download from **http://sholl.chbe.gatech.edu/databases.html**. **Fig. 7** illustrates the types of structures in the database for each Miller index. **Fig. 7a** shows a CAS (001) slab termination pair along with the CAS (001) LRUC. The pair of upper and lower surfaces have been relaxed as described above and can be stacked around any number of LRUCs to make a slab with any height of interest. This approach is well suited for simulations on large structures where framework flexibility is neglected. **Fig. 7b** shows CAS (001) slabs of varying heights. These slabs do not have relaxed surfaces and are intended for simulations in which frame-

work flexibility would be included. They are meant to resemble the nanosheets obtained experimentally using modified structure-directing agents.[5]

Fig. 8 compares known nanosheets from previous experimental reports and their slab counterparts from the database. The experimental structures were obtained from Rietveld-type refinements of XRD patterns, usually of zeolite layer precursors.[45-55] Two exceptions to this were IPC-1 and MFI, for which no refined structures could be found. The IPC-1 structure displayed was derived from a comparison of XRD pattern peaks before and after calcination.[56, 57] For MFI, an SEM image was used.[5]

The refined precursor structures usually contained structure directing agent cations which were edited out of the images in **Fig. 8** for clarity. The slabs were chosen by visually comparing slabs in the database to cross-sectional images of the refined structures. The close agreement between the experimental data and the slabs is an indication that the procedures we used yield physically meaningful results. Though the resemblance was close overall, some nanosheets seemed to deviate more from their slab counterpart than others. Most notably, PKU-22 appears less atomically dense in the center of the structure. Experimentally, PKU-22 contains F- anions (cyan) bonded to Ge T-sites,[45] so this is likely why it looks slightly dissimilar from the all-silica database nanosheet. For MFI, it is notable that the thickness of the silica section of the SEM (2 nm) and the database slab with the lowest number of broken bonds on the surface (2.2 nm) were roughly equivalent.[5] The difference in heights could be due the difficulty of identifying the exact termination point of the MFI silica layer in the SEM image.
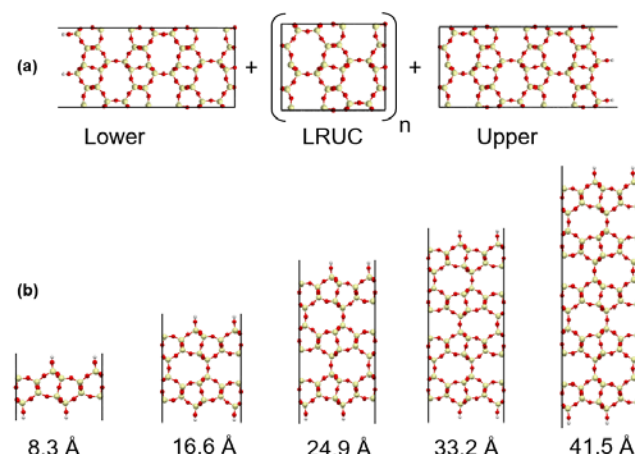
Figure 7. (a) A slab termination pair with a relaxed surface and the LRUC for CAS (001). (b) CAS (001) Slabs with set height and unrelaxed surfaces.

The only other comprehensive 2D zeolite database to our knowledge is that of Witman et al.[26] That database only includes 3,682 slabs, all with surfaces that minimize the number of broken bonds and are more than 30 Å thick.[26] For example, the Witman et al. CAS (001) slab is slightly taller than the 41.5 Å slab in **Fig. 7(b)** and far thicker than the CAS nanosheet in **Fig. 8**. A key advantage of the present database is that it has structures representative of nanosheets of variable height. In addition, Witman et al. limited their attention to only those
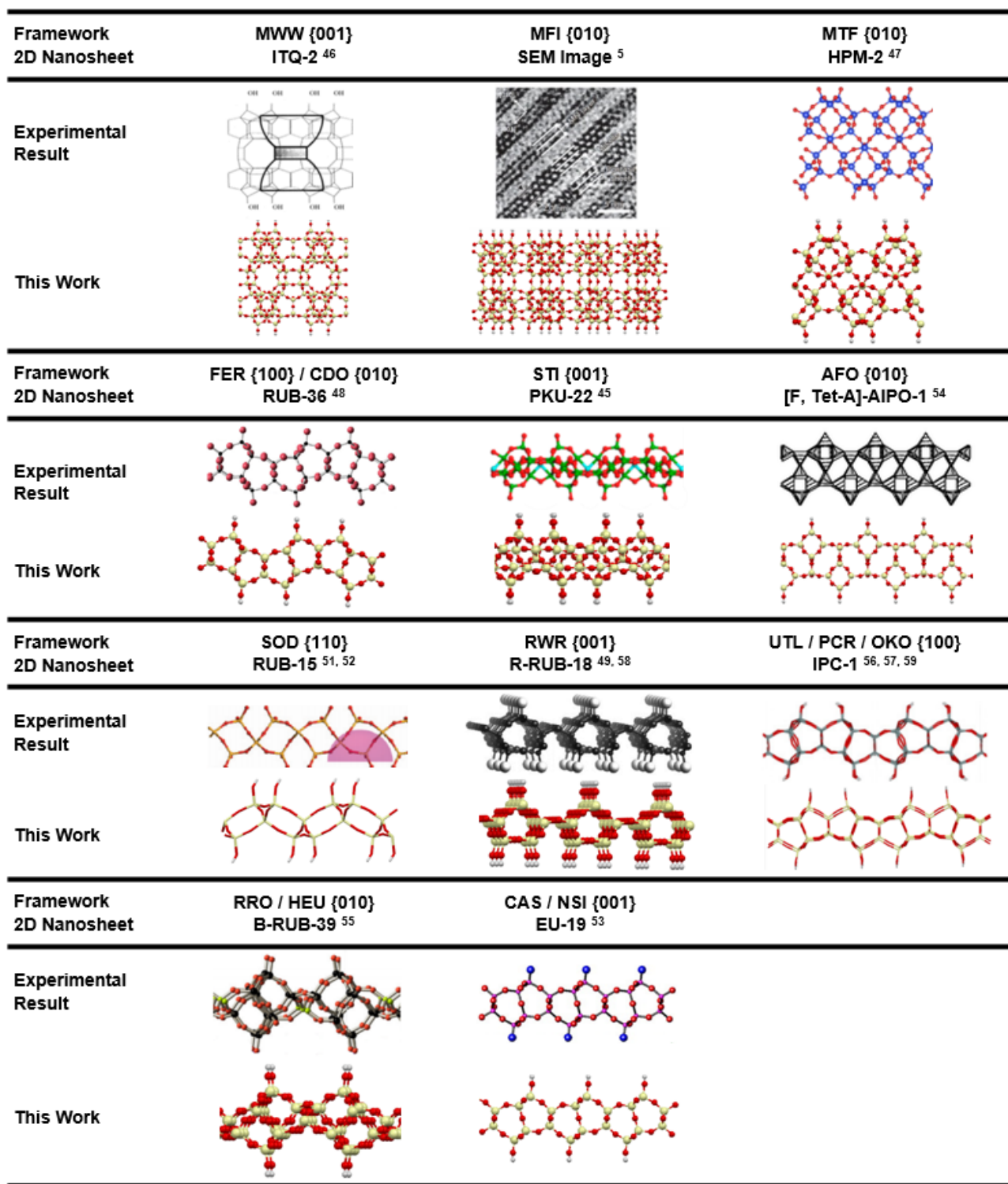
Figure 8. A comparison of experimentally obtained nanosheets with their database counterparts. The MFI SEM image was adapted by permission from Nature Springer: Nature (Stable single-unit-cell nanosheets of zeolite MFI as active and long-lived catalysts, Choi, Minkee, et al.), copyright 2009.[5]   R-RUB-18 was adapted from Microporous and Mesoporous Materials, Vol 83(1),   Marler, B., N. Ströter, and H. Gies, The structure of the new pure silica zeolite RUB-24, $Si_{32}O_{64}$, obtained by topotactic condensation of the intercalated layer silicate RUB-18, p. 201-211, copyright 2005 with permission from Elsevier.[62] IPC-1 was adapted from Catalysis Today, Vol. 204, Grajciar, L., et al., Theoretical investigation of layered zeolite frameworks: Interaction between IPC-1P layers derived from zeolite UTL, p. 15-21, copyright 2013 with permission from Elsevier.[56] EU-19 was adapted from Microporous and Mesoporous Materials, Vol 90(1), Marler, B., M. Camblor, and H. Gies, The disordered structure of silica zeolite EU-20b, obtained by topotactic condensation of the piperazinium containing layer silicate EU-19, p. 87-101, copyright 2006 with permission from Elsevier.[53]   B-RUB-39 was adapted from Microporous and Mesoporous Materials, Vol 147(1), Grünewald-Lüke, A., et al.,   Layered precursors for new zeolitic materials: Synthesis and characterization of B-RUB-39 and its condensation product   B-RUB-41,   p.   102-109,   copyright   2012   with   permission   from   Elsevier.[55]

surfaces with the minimum number of broken bonds, hindering the ability to consider the effects of different surfaces with the same Miller index. As noted in **Fig. S1**, the surface with the minimum number of broken bonds does not always result in the surface with the lowest surface energy. It is also noteworthy that the graph theory method of Witman et al. could readily be augmented to produce surfaces with a higher broken bond tolerance.[26]

WULFF CONSTRUCTIONS

Crystal Habit Prediction Method. One immediate use of our database is to predict the equilibrium crystal habit of zeolite crystals. Here we do this using the Wulff construction,[58] which minimizes the surface energy of a crystal.[58] Crystal habit can of course be influenced by the kinetics of crystal growth, but modeling of this situation must incorporate details of nucleation and growth that are beyond the scope of our work. While work by Anderson et al. has shown that simulation of kinetically-controlled zeolite crystal growth is possible,[59] it is not feasible to apply these methods to a broad range of materials and growth conditions. We therefore focus here on using the Wulff construction to provide the first comprehensive description of equilibrium zeolite crystal habits.

The surface energy of an -OH terminated zeolite surface is a measure of the thermodynamic favorability of the bulk relative to the surface and is defined as:[60]

$$\gamma_{Reaxff} = \frac{1}{2A}(E_{slab} - r \times E_{bulk} - n \times \mu_{water})$$ **1**

where γ is the surface energy, A is the surface area, E_{slab} is the minimized energy of the nanosheet, r the number of Si atoms in the slab divided by the number of Si atoms in the bulk, E_{bulk} is the minimized energy of the bulk, n is the number of water molecules added to terminate the structure, and μ_{water} is the chemical potential of liquid water. We used the chemical potential of water at 0 K, found by subtracting the condensation energy at 100 °C from the minimized energy of a gaseous water molecule.[61] Estimating the chemical potential by simulating bulk liquid water using ReaxFF gave a very similar value. Minimized energies for each surface were obtained from the relaxed slab prior to splitting slabs into top and bottom terminations. Because we defined slabs in which the upper and lower surfaces were related by symmetry, the surface energy can be unambiguously assigned to each surface, unlike the situation that arises when the top and bottom of a slab are not identical. The minimized energy for gaseous water was obtained from relaxation of a single water molecule in a large computational volume with ReaxFF in LAMMPS.[32, 33] It is important to note that the use of a force field such as ReaxFF that allows for bond formation and breaking is critical to computing the surface energy of these surfaces. Simpler force fields such as the Hill-Sauer force field allow the simulation of -OH terminated zeolites,[41] but cannot be used to self-consistently compare the relative energy required to hydrate a variety of surfaces.

Since the number of broken bonds has a large impact on surface energy, surface energy can also be estimated by dividing the number of broken bonds by the surface area:[26]

$$\gamma_{estimate} = \frac{N_{BrokenBonds}}{2A}$$ **2**

The Pymatgen software package was used to generate the Wulff constructions for each material.[35] It took as input a list of Miller indices and their respective surface energies for all Miller indices with MMI < 3. Two sets of Wulff constructions were generated, one using γ_{reaxff} and one using $\gamma_{estimate}$. For both cases, the surface energy used to represent a Miller index was the minimum surface energy calculated amongst all surfaces on that Miller index. The resulting Wulff shapes for each zeolite are available for download from **http://sholl.chbe.gatech.edu/databases.html**.

Several of the Wulff constructions obtained from our calculations are compared to SEM images of zeolite crystals from previous reports in **Figs. 9-10**. The zeolites shown in these figures exhibited a range of crystal habits. For each framework, an SEM image of a single crystal, a Wulff shape based on $\gamma_{estimate}$, and a Wulff shape based on γ_{reaxff} are shown respectively. Each Wulff shape also has a legend which contains the surface area percentage occupied by each Miller index. The results were sorted between **Figs. 9 and 10** depending on the level of resemblance between the experimentally observed crystal and the predicted Wulff shapes. If the Miller indices that are dominant on the experimentally reported crystal are also dominant on one of the two Wulff constructions, the framework is displayed in **Fig. 9**. If Miller indices dominant on the experimentally reported crystal are not dominant on either Wulff construction, the framework is displayed in **Fig. 10**. We reiterate that the Wulff constructions included all Miller index surfaces with MMI < 3. Frequently, only a subset of the surfaces considered are predicted to actually be expressed on the crystal habit. For example, our calculations for ANA included the {100}, {110}, {111}, {210}, {211} and {221} surfaces, but only the {100} and {211} surfaces appear on the Wulff shape generated using $\gamma_{estimate}$. Similarly, the Wulff construction for NAT includes the {001}, {100}, {101}, {102}, {110}, {112}, {201}, {210}, {211} and {221} surfaces, but only the {100} and {101} surfaces appear on the Wulff shape from $\gamma_{estimate}$.

One observation from **Figs. 9 and 10** is that the Wulff shapes based on $\gamma_{estimate}$ resembled the SEM images more than Wulff shapes based on γ_{reaxff}. In **Fig. 9**, the GME, MER, ANA, and MFI Wulff shapes based on $\gamma_{estimate}$ are similar, although not identical to the experimental images. In **Fig. 10**, the GIS and NAT Wulff shapes based on $\gamma_{estimate}$ show resemblance to the experimentally reported crystals while those of LTA and ABW do not, so it may seem at first glance that GIS and NAT should be in **Fig. 9**. Closer inspection of GIS shows that while the {111} surface is dominant on the experimentally reported crystal, the {101} surface is dominant on the Wulff shape. A similar scenario is observed in NAT, where the {110} and {111} surfaces dominate the observed crystal while the {100} and {101} Miller index groups dominate the Wulff shape.

Experimental Observation	Wulff Shape based on $\gamma_{estimate}$	Wulff Shape based on γ_{Reaxff}

GME

{101} : 61
{100} : 39

{001} {100} {101}
{102} {110} {111} {2$\overline{1}$2} {201} {210} {211} {212} {221}

Precursor Si/Al: 2

{101} : 45
{211} : 26
{111} : 19
{100} : 6
{212} : 4

MER

{100} : 53
{101} : 46
{112} : 1

{001} {100} {101}
{102} {110} {111} {112} {201} {210} {211} {212} {221}

Crystal Si/Al: 2

{211} : 50
{111} : 25
{101} : 13
{100} : 9
{212} : 4

ANA

{100} : 62
{211} : 38

{100} {110} {111}
{210} {211} {221}

Crystal Si/Al: 1.8

{110} : 71
{211} : 22
{111} : 8

MFI

{010} : 26
{100} : 26
{011} : 24
{101} : 24

{001} {010} {011} {012} {021} {100} {101} {102}
{110} {111} {112} {120} {121} {122} {201} {210}
{211} {212} {221}

Crystal Si/Al: 19

{101} : 21
{121} : 16
{011} : 14
{110} : 12
{210} : 8
{111} : 7
{010} : 7
{100} : 5
{211} : 3
{120} : 3
{221} : 2
{201} : 2
{021} : 1

Figure 9. For each framework, an SEM image (left), a $\gamma_{estimate}$ Wulff shape (center), and a γ_{reaxff} Wulff shape (right) is shown. The Wulff shape legends show the surface area (%) occupied by each Miller index. The Miller indices used to generate both Wulff constructions listed below the Wulff shapes. GME was adapted from Agewandte Chemie, Vol 40(20), Ghobarkar, Habib, Oliver Schäf, and Philippe Knauth, Zeolite Synthesis by the High-Pressure Hydrothermal Method: Synthesis of Natural 6-Ring Zeolites with Different Void Systems, p. 3831-3833, copyright 2001 with permission from John Wiley and Sons.[68] MER was adapted from the Journal of Industrial and Engineering Chemistry, Vol 20(4), Jin, Na, Chunxia Meng, and Jin Hou, Preparation and characterization of merlinoite for potassium extraction from seawater, p. 1227-1230, copyright 2014 with permission from Elsevier.[69] ANA was adapted from Materials Science and Engineering, Vol 60(3), Ghobarkar, H., and O. Schäf, Effect of temperature on hydrothermal synthesis of analcime and viséite, p. 163-167, copyright 1999 with permission from Elsevier.[70] MFI was adapted from Chemistry of Materials.[71]
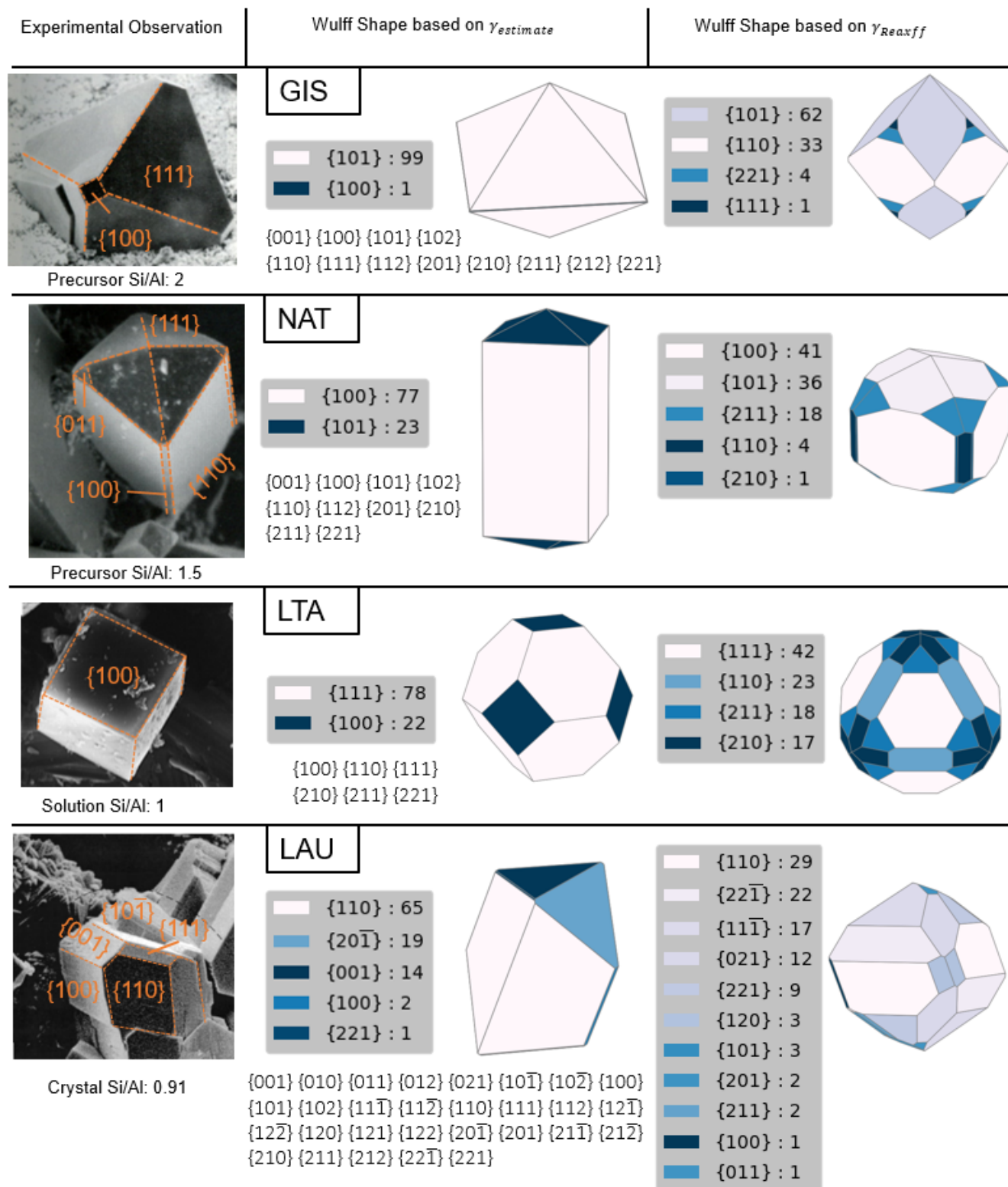
Figure 10. For each framework, an SEM image (left), a $\gamma_{estimate}$ Wulff shape (center), and a γ_{reaxff} Wulff shape (right) is shown. The Wulff shape legends show the surface area (%) occupied by each Miller index. The Miller indices used to generate both Wulff constructions listed under below the Wulff shapes. GIS was adapted from the Materials Research Buttetin, Vol 34(4), Ghobarkar, H., and O. Schäf, Synthesis of gismondine-type zeolites by the hydrothermal method, p. 517-525, copyright 1999 with permission from Elsevier.[72] NAT was adapted by permission from Springer Nature: American Chemical Society, The Reconstruction of Natural Zeolites, p. 43, by Ghobarkar, Habbib, Oliver Schaf, and Yvan Massiani, copyright 2003.[73] LTA was adapted from Materials Letters, Vol 34(3-6), Basaldella, Elena, and J. C. Tara, Modification of crystallite morphology during synthesis of LTA zeolite using triethanolamine as additive, 119-123, copyright 1998 with permission from Elsevier.[64] LAU was adapted from the Microporous and Mesoporous Materials, Vol 23(1-2), Ghobarkar, H., and O. Schäf, Hydrothermal synthesis of laumonite, a zeolite, p. 55-60, copyright 1998 with permission from Elsevier.[74]

Finally, we note that our algorithm did not find the correct minimum cut for MER {212}. When we rebuilt the Wulff construction based on $\gamma_{estimate}$ using 20 bonds broken for the {212} Miller index (the correct number of minimum bonds as identified by Witman et al.)[26], instead of 22 bonds broken, we obtained the same Wulff shape shown in **Fig. 9**. The {212} surface did not appear.

A second observation from **Figs. 9 and 10** is that the experimental crystals and Wulff shapes based on $\gamma_{estimate}$ are dominated by lower Miller indices (ex. {100}, {101}) while those based on γ_{reaxff} exhibit many high Miller index surfaces (ex. {212}, {210}). We believe this to be because our surfaces are relaxed in vacuum rather than in water. Experimentally, surface silanol groups form hydrogen bonds with water.[44] Since this cannot occur in our vacuum simulations, surface silanol groups form hydrogen bonds with themselves as shown in **Fig. 6(d)**. Therefore, the surfaces that form more hydrogen bonds are likely to obtain lower surface energies. Incidentally, the LRUC of high Miller index surfaces are often non-orthogonal, so H atoms (which are located vertically above the O in orthogonal unit cells as seen in **Fig. 3(e)**) are located diagonally above the O in non-orthogonal unit cells as seen in **Fig. 6(d)**). The location of H atoms in high Miller index unit cells facilitates the formation of hydrogen bonds and therefore lowers the surface energy of the high Miller index surfaces without the corresponding decrease in surface energy that would have occurred in lower Miller index unit cells due to interactions with water.

The subtleties associated with comparing our Wulff shapes with experimental results are highlighted by previous work by Gren et al., who simulated siliceous and aluminosilicate LTA surfaces.[61] They found that the presence of Al stabilizes the {100} surface relative to the {111} surface, and that this trend is further exacerbated by the presence of liquid water. The resulting pure silica crystal was rounded while their Si/Al=1 crystal was cubic.[61] Therefore, their predicted Si/Al=1 crystal morphology resembles that of most experimental crystals.[63-66] Although the surface energies of our siliceous slabs give different relative surface energies than those obtained by Gren et al. for aluminosilicates, the structure of the low energy surfaces found by Gren et al. and the surfaces from our calculations are very similar (see **Figure S7**). The materials shown in **Figs. 9** and 10 are all aluminosilicates, but those in **Fig. 9** generally have a higher Si:Al ratio than those in **Fig. 10**. The Si:Al ratios refer to either the precursor, solution, or crystal Si:Al ratios. The precursor Si:Al ratio refers to the composition of glass which was melted and quenched with water during hydrothermal synthesis to form the final crystal.[68] The LAU crystal's 0.9 Si:Al ratio is likely less than one solely due to the elemental analysis' accuracy of 10%.[74] Since our database is pure silica, it is not surprising that the zeolites with higher Si:Al ratio bear more resemblance to the known structures.

It is interesting to examine the ability of the calculated surface energies from our database to predict the specific surfaces that appear on the experimentally known nanosheets shown in **Fig. 8**. For each of the 16 experimentally reported nanosheets, the surface of the framework with the lowest $\gamma_{estimate}$ and γ_{reaxff} was chosen from the set of all surfaces belonging to that framework as the prediction from our database for the surface that would be observed as a nanosheet. For 13 of the 16 frameworks, the surface defined by both $\gamma_{estimate}$ and γ_{reaxff} was the same as the experimentally reported material. For 2 of the 13 frameworks, UTL and OKO, there were two surfaces (identical in both frameworks because they are formed from the same zeolite layer precursor)[75] with equal $\gamma_{estimate}$ values. In these cases, γ_{reaxff} gives slightly different surface energies and the prediction based on the lowest of these energies is the same as the experimentally reported surface. For the remaining 3 frameworks, MFI, SOD, and RWR, the surface indicated by $\gamma_{estimate}$ differed from that using γ_{reaxff}. For MFI, the surface indicated by $\gamma_{estimate}$ correctly matches the (010) orientation seen experimentally (noting that the exact termination has not been determined experimentally to date).[5] However, the MFI surface indicated by γ_{reaxff} displayed a {101} Miller index. For RWR, the surface indicated by $\gamma_{estimate}$ was seen on the experimentally observed nanosheet while the surface indicated by γ_{reaxff} was not. SOD is the only structure for which the surface indicated by $\gamma_{estimate}$, a {100} surface, was not seen experimentally, although the {110} surface observed on the nanosheet was indicated by γ_{reaxff}. The above discussion shows that the surface with the lowest $\gamma_{estimate}$ and γ_{reaxff} is most likely to be observed experimentally in zeolitic nanosheets. Although this was not the case with the MFI {101} and SOD {100} surfaces predicted by γ_{reaxff} and $\gamma_{estimate}$ respectively, those surfaces are observed on their framework's bulk crystal habit.[76, 77] The identification of the experimental nanosheet surfaces in most instances by $\gamma_{estimate}$ concurs with Witman's results which assume that the surface with the lowest $\gamma_{estimate}$ will be seen on the nanosheet.[26] We combine this information, along with the finding that the γ_{reaxff} can break a $\gamma_{estimate}$ tie to produce a shortlist (in the zipped file) of the 217 most likely zeolite surfaces to be synthesized as a nanosheet.

CONCLUSIONS

We have created a very large database of 2D zeolite nanosheets which can form the basis for systematic studies of the functional properties (e.g., diffusion, adsorption, catalytic) of this rapidly emerging class of nanoporous materials. We first formed surfaces using an algorithm that iteratively removed undercoordinated atoms to find terminations with a low number of broken bonds. The selected surfaces were screened for symmetry and uniqueness then combined to form slabs. The database currently contains 651,850 2D zeolitic slabs and 152,992 slab termination pairs. The slabs have set thicknesses (1-15 nm) and contain nanosheets with the same thicknesses as those found experimentally. The slab termination pairs can form structures with thicknesses greater than those spanned by the slabs. Our database can therefore be used to study nanosheet properties as a function of thickness and surface structure, a feature that is unique to the current work. We used surface energies obtained using the ReaxFF force field and surface energies obtained from broken bond densities to predict the crystal morphology

of zeolite crystals and the surfaces observed on nanosheets. The broken bond density predicted more accurate crystal structures while both metrics were equally favorable at predicting which surfaces are present on a nanosheet.

It is important to note that our 2D zeolite structures are pure silica materials, and that our calculated surface energies do not include the solvent effects that are certain to be present during zeolite synthesis. As discussed above, examples are known in which variations in the Si:Al ratio and/or inclusion of solvent effects can alter the relative surface energy ordering of surfaces on zeolites. Despite the complications associated with these effects, we were able to narrow the list of surfaces to those most likely to be synthesizable. We hope that this subset can be used to identify synthesized slabs in a high throughput way, such as the matching of theoretical to experimental XRD patterns. Alternatively, we foresee its use in the screening of structure directing agents to identify those best suited to form a particular slab. Finally, our database of atomically detailed structures will be valuable for molecular simulations of zeolitic nanosheets that aim to understand how the performance of these materials differs from bulk materials.

ASSOCIATED CONTENT

Supporting Information. Maximum Miller index table, cell dimensions post relaxation, MFI surface terminations, surface naming procedure, broken bond tolerance graph, cell symmetry explanation, radial distribution function, discontinuity figure, assembly and disassembly of slabs before and after relaxation, simulated annealing graph, LTA surface comparison, software.

AUTHOR INFORMATION

Corresponding Author

* E-mail: david.sholl@chbe.gatech.edu.

Author Contributions

The authors jointly conceived the study and analyzed the results. O.K. developed the underlying code, performed all numerical calculations, and formatted the data that is reported.

Notes
The authors declare no competing financial interests.

ACKNOWLEDGMENT

REFERENCES

1. Sholl, D.S. and R.P. Lively, *Seven chemical separations to change the world.* Nature, 2016. **532**(7600): p. 435.

2. Walton, K.S. and D.S. Sholl, *Research Challenges in Avoiding "Showstoppers" in Developing Materials for Large-Scale Energy Applications.* Joule, 2017. **1**(2): p. 208-211.

3. Feng, C., K. Khulbe, T. Matsuura, R. Farnood, and A. Ismail, *Recent progress in zeolite/zeotype membranes.* J. Membr. Sci. Res., 2015. **1**(2): p. 49-72.

4. Rangnekar, N., N. Mittal, B. Elyassi, J. Caro, and M. Tsapatsis, *Zeolite membranes–a review and comparison with MOFs.* Chem. Soc. Rev., 2015. **44**(20): p. 7128-7154.

5. Choi, M., K. Na, J. Kim, Y. Sakamoto, O. Terasaki, and R. Ryoo, *Stable single-unit-cell nanosheets of zeolite MFI as active and long-lived catalysts.* Nature, 2009. **461**(7261): p. 246-249.

6. Luo, H.Y., V.K. Michaelis, S. Hodges, R.G. Griffin, and Y. Román-Leshkov, *One-pot synthesis of MWW zeolite nanosheets using a rationally designed organic structure-directing agent.* Chem. Sci., 2015. **6**(11): p. 6320-6324.

7. Rangnekar, N., M. Shete, K.V. Agrawal, B. Topuz, P. Kumar, Q. Guo, I. Ismail, A. Alyoubi, S. Basahel, and K. Narasimharao, *2D zeolite coatings: Langmuir–Schaefer deposition of 3 nm thick MFI zeolite nanosheets.* Angew. Chem., Int. Ed., 2015. **54**(22): p. 6571-6575.

8. Fasano, M., T. Humplik, A. Bevilacqua, M. Tsapatsis, E. Chiavazzo, E.N. Wang, and P. Asinari, *Interplay between hydrophilicity and surface barriers on water transport in zeolite membranes.* Nat. Commun., 2016. **7**: p. 12762.

9. Newsome, D.A. and D.S. Sholl, *Predictive assessment of surface resistances in zeolite membranes using atomically detailed models.* J. Phys. Chem. B, 2005. **109**(15): p. 7237-7244.

10. Newsome, D.A. and D.S. Sholl, *Atomically detailed simulations of surface resistances to transport of CH_4, CF_4, and C_2H_6 through silicalite membranes.* Microporous and Mesoporous Mater., 2008. **107**(3): p. 286-295.

11. Teixeira, A.R., C.-C. Chang, T. Coogan, R. Kendall, W. Fan, and P.J. Dauenhauer, *Dominance of surface barriers in molecular transport through silicalite-1.* J. Phys. Chem. C, 2013. **117**(48): p. 25545-25555.

12. Teixeira, A.R., X. Qi, W.C. Conner, T. Mountziaris, W. Fan, and P.J. Dauenhauer, *2D surface structures in small zeolite MFI crystals.* Chem. Mater., 2015. **27**(13): p. 4650-4660.

13. Vattipalli, V., X. Qi, P.J. Dauenhauer, and W. Fan, *Long walks in hierarchical porous materials due to combined surface and configurational diffusion.* Chem. Mater., 2016. **28**(21): p. 7852-7863.

14. Tzoulaki, D., W. Schmidt, U. Wilczok, and J. Kärger, *Formation of surface barriers on silicalite-1 crystal fragments by residual water vapour as probed with isobutane by interference microscopy.* Microporous and Mesoporous Mater., 2008. **110**(1): p. 72-76.

15. Li, L., N. Liu, B. McPherson, and R. Lee, *Enhanced water permeation of reverse osmosis through MFI-type zeolite membranes with high aluminum contents.* Industrial & engineering chemistry research, 2007. **46**(5): p. 1584-1589.

16. Baerlocher, C. and McCusker, L. IZA database of zeolite structures. http://www.iza-structure.org/databases/. Accessed 3 September 2017

17. Baerlocher, C., A. Hepp, and W.M. Meier, *DLS-76: A Program for the Simulation of Crystal Structures by Geometric Refinement.* revised ed. 1978: Institute of crystallography and petrography - ETH.

18. Wang, Z., J. Yu, and R. Xu, *Needs and trends in rational synthesis of zeolitic materials.* Chem. Soc. Rev., 2012. **41**(5): p. 1729-1741.

19. Treacy, M., S. Rao, and I. Rivin, *A combinatorial method for generating new zeolite frameworks.* R. von Ballmoos, JB Higgins, MMJ Treacy (Eds.), 1992: p. 381-388.

20. Treacy, M., I. Rivin, E. Balkovsky, K. Randall, and M. Foster, *Enumeration of periodic tetrahedral frameworks. II. Polynodal graphs.* Microporous and Mesoporous Mater., 2004. **74**(1): p. 121-132.

21. Corma, A., M.J. Díaz-Cabañas, J.L. Jordá, C. Martínez, and M. Moliner, *High-throughput synthesis and catalytic properties of a molecular sieve with 18-and 10-member rings.* Nature, 2006. **443**(7113): p. 842-845.

22. Jiang, J., J.L. Jorda, M.J. Diaz-Cabanas, J. Yu, and A. Corma, *The Synthesis of an Extra-Large-Pore Zeolite with*

Double Three-Ring Building Units and a Low Framework Density. Angew. Chem., Int. Ed., 2010. **49**(29): p. 4986-4988.

23. Friedrichs, O.D., A.W. Dress, D.H. Huson, J. Klinowski, and A.L. Mackay, *Systematic enumeration of crystalline networks.* Nature, 1999. **400**(6745): p. 644-647.

24. Pophale, R., P.A. Cheeseman, and M.W. Deem, *A database of new zeolite-like materials.* Phys. Chem. Chem. Phys., 2011. **13**(27): p. 12407-12412.

25. Jamali, S.H., T.J. Vlugt, and L.-C. Lin, *Atomistic understanding of zeolite nanosheets for water desalination.* J. Phys. Chem. C, 2017. **121**(21): p. 11273-11280.

26. Witman, M., S. Ling, P. Boyd, S. Barthel, M. Haranczyk, B. Slater, and B. Smit, *Cutting Materials in Half: A Graph Theory Approach for Generating Crystal Surfaces and Its Prediction of 2D Zeolites.* ACS. Cent. Sci., 2018. 4(2): p. 235-245

27. Habib Ghobarkar, O.S., Yvan Massiani, Philippe Knauth, *The reconstruction of natural zeolites.* 2003: Kluwer Academic Publishers. 146.

28. Gounaris, C.E., C.A. Floudas, and J. Wei, *Rational design of shape selective separation and catalysis—I: Concepts and analysis.* Chem. Eng. Sci., 2006. **61**(24): p. 7933-7948.

29. Gounaris, C.E., J. Wei, and C.A. Floudas, *Rational design of shape selective separation and catalysis—II: Mathematical model and computational studies.* Chem. Eng. Sci., 2006. **61**(24): p. 7949-7962.

30. Haldoupis, E., S. Nair, and D.S. Sholl, *Efficient calculation of diffusion limitations in metal organic framework materials: a tool for identifying materials for kinetic separations.* J. Am. Chem. Soc., 2010. **132**(21): p. 7528-7539.

31. Haldoupis, E., S. Nair, and D.S. Sholl, *Finding MOFs for highly selective CO_2/N_2 adsorption using materials screening based on efficient assignment of atomic point charges.* J. Am. Chem. Soc., 2012. **134**(9): p. 4313-4323.

32. Fogarty, J.C., H.M. Aktulga, A.Y. Grama, A.C. Van Duin, and S.A. Pandit, *A reactive molecular dynamics simulation of the silica-water interface.* J. Chem. Phys., 2010. **132**(17): p. 174704.

33. Brown, W.M., P. Wang, S.J. Plimpton, and A.N. Tharrington, *Implementing molecular dynamics on hybrid high performance computers–short range forces.* Comput. Phys. Commun., 2011. **182**(4): p. 898-911.

34. Senftle, T.P., S. Hong, M.M. Islam, S.B. Kylasa, Y. Zheng, Y.K. Shin, C. Junkermeier, R. Engel-Herbert, M.J. Janik, and H.M. Aktulga, *The ReaxFF reactive force-field: development, applications and future directions.* npj Comput. Mater., 2016. **2**: p. 15011.

35. Tran, R., Z. Xu, B. Radhakrishnan, D. Winston, W. Sun, K.A. Persson, and S.P. Ong, *Surface energies of elemental crystals.* Sci. Data, 2016. **3**: p. 160080.

36. Lunevich, L., P. Sanciolo, A. Smallridge, and S. Gray, *Silica scale formation and effect of sodium and aluminium ions-29 Si NMR study.* Environ. Sci.: Water Res. Technol., 2016. **2**(1): p. 174-185.

37. Slater, B., J. Titiloye, F. Higgins, and S. Parker, *Atomistic simulation of zeolite surfaces.* Curr. Opin. Solid State Mater. Sci., 2001. **5**(5): p. 417-424.

38. Verploegh, R.J., S. Nair, and D.S. Sholl, *Temperature and loading-dependent diffusion of light hydrocarbons in ZIF-8 as predicted through fully flexible molecular simulations.* J. Am. Chem. Soc., 2015. **137**(50): p. 15760-15771.

39. Krishna, R. and J.M. Van Baten, *A molecular dynamics investigation of the diffusion characteristics of cavity-type zeolites with 8-ring windows.* Microporous and Mesoporous Mater., 2011. **137**(1): p. 83-91.

40. de Leeuw, N.H., F.M. Higgins, and S.C. Parker, *Modeling the surface structure and stability of α-quartz.* J. Phys. Chem. B, 1999. **103**(8): p. 1270-1277.

41. Hill, J.R. and J. Sauer, *Molecular mechanics potential for silica and zeolite catalysts based on ab initio calculations. 1. Dense and microporous silica.* J. Phys. Chem., 1994. **98**(4): p. 1238-1244.

42. Sanders, M., M. Leslie, and C. Catlow, *Interatomic potentials for SiO_2.* J. Chem. Soc., Chem. Commun., 1984(19): p. 1271-1273.

43. Zang, J., S. Chempath, S. Konduri, S. Nair, and D.S. Sholl, *Flexibility of ordered surface hydroxyls influences the adsorption of molecules in single-walled aluminosilicate nanotubes.* J. Phys. Chem. Lett., 2010. **1**(8): p. 1235-1240.

44. Chuang, I.-S. and G.E. Maciel, *Probing hydrogen bonding and the local environment of silanols on silica surfaces via nuclear spin cross polarization dynamics.* J. Am. Chem. Soc., 1996. **118**(2): p. 401-406.

45. Chen, Y., S. Huang, X. Wang, L. Zhang, N. Wu, F. Liao, and Y. Wang, *Synthesis and Characterization of a Layered Silicogermanate PKU-22 and Its Topotactic Condensation to a Three-Dimensional STI-type Zeolite.* Cryst. Growth Des., 2017. **17**(10): p. 5465-5473.

46. Narkhede, V.V. and H. Gies, *Crystal structure of MCM-22 (MWW) and its delaminated zeolite ITQ-2 from high-resolution powder X-ray diffraction data: an analysis using Rietveld technique and atomic pair distribution function.* Chem. Mater., 2009. **21**(18): p. 4339-4346.

47. Rojas, A. and M.A. Camblor, *HPM-2, the layered precursor to zeolite MTF.* Chem. Mater., 2014. **26**(2): p. 1161-1169.

48. Gies, H., U. Müller, B. Yilmaz, M. Feyen, T. Tatsumi, H. Imai, H. Zhang, B. Xie, F.-S. Xiao, and X. Bao, *Interlayer expansion of the hydrous layer silicate RUB-36 to a functionalized, microporous framework silicate: crystal structure analysis and physical and chemical characterization.* Chem. Mater., 2012. **24**(8): p. 1536-1545.

49. Vortmann, S., J. Rius, S. Siegmann, and H. Gies, *Ab initio structure solution from X-ray powder data at moderate resolution: crystal structure of a microporous layer silicate.* J. Phys. Chem. B, 1997. **101**(8): p. 1292-1297.

50. Marler, B., N. Ströter, and H. Gies, *The structure of the new pure silica zeolite RUB-24, $Si_{32}O_{64}$, obtained by topotactic condensation of the intercalated layer silicate RUB-18.* Microporous and Mesoporous Mater., 2005. **83**(1): p. 201-211.

51. Moteki, T., W. Chaikittisilp, Y. Sakamoto, A. Shimojima, and T. Okubo, *Role of acidic pretreatment of layered silicate RUB-15 in Its topotactic conversion into pure silica sodalite.* Chem. Mater., 2011. **23**(15): p. 3564-3570.

52. Oberhagemann, U., P. Bayat, B. Marler, H. Gies, and J. Rius, *A Layer Silicate: Synthesis and Structure of the Zeolite Precursor RUB-15—$[N(CH_3)_4]_8[Si_{24}O_{52}(OH)_4]\cdot 20\ H_2O$.* Angew. Chem., Int. Ed., 1996. **35**(23-24): p. 2869-2872.

53. Marler, B., M. Camblor, and H. Gies, *The disordered structure of silica zeolite EU-20b, obtained by topotactic condensation of the piperazinium containing layer silicate EU-19.* Microporous and Mesoporous Mater., 2006. **90**(1): p. 87-101.

54. Wheatley, P.S. and R.E. Morris, *Calcination of a layered aluminofluorophosphate precursor to form the zeolitic AFO framework.* J. Mater. Chem., 2006. **16**(11): p. 1035-1037.

55. Grünewald-Lüke, A., H. Gies, U. Müller, B. Yilmaz, H. Imai, T. Tatsumi, B. Xie, F.-S. Xiao, X. Bao, and W. Zhang, *Layered precursors for new zeolitic materials: Synthesis and characterization of B-RUB-39 and its condensation product B-RUB-41.* Microporous and Mesoporous Mater., 2012. **147**(1): p. 102-109.

56. Grajciar, L., O. Bludský, W.J. Roth, and P. Nachtigall, *Theoretical investigation of layered zeolite frameworks: Interaction between IPC-1P layers derived from zeolite UTL.* Catal. Today, 2013. **204**: p. 15-21.

57. Roth, W.J., O.V. Shvets, M. Shamzhy, P. Chlubná, M. Kubů, P. Nachtigall, and J.i. Čejka, *Postsynthesis transformation of three-dimensional framework into a lamellar zeolite with modifiable architecture.* J. Am. Chem. Soc., 2011. **133**(16): p. 6130-6133.

58. Ringe, E., R. Van Duyne, and L. Marks, *Wulff construction for alloy nanoparticles.* Nano Lett., 2011. **11**(8): p. 3399-3403.

59. Anderson, M.W., J.T. Gebbie-Rayet, A.R. Hill, N. Farida, M.P. Attfield, P. Cubillas, V.A. Blatov, D.M. Proserpio, D. Akporiaye, and B. Arstad, *Predicting crystal growth via a unified kinetic three-dimensional partition model.* Nature, 2017. **544**(7651): p. 456.

60. De Leeuw, N., S. Parker, C. Catlow, and G. Price, *Modelling the effect of water on the surface structure and stability of forsterite.* Phys. Chem. Miner., 2000. **27**(5): p. 332-341.

61. Gren, W., S.C. Parker, B. Slater, and D.W. Lewis, *Structure of zeolite A (LTA) surfaces and the zeolite A/water interface.* J. Phys. Chem. C, 2010. **114**(21): p. 9739-9747.

62. Marler, B., N. Ströter, and H. Gies, *The structure of the new pure silica zeolite RUB-24, $Si_{32}O_{64}$, obtained by topotactic condensation of the intercalated layer silicate RUB-18.* Microporous and Mesoporous Mater., 2005. **83**(1): p. 201-211.

63. Bouizi, Y., J.-L. Paillaud, L. Simon, and V. Valtchev, *Seeded synthesis of very high silica zeolite A.* Chem. Mater., 2007. **19**(4): p. 652-654.

64. Basaldella, E.I. and J. Tara, *Modification of crystallite morphology during synthesis of LTA zeolite using triethanolamine as additive.* Mater. Lett., 1998. **34**(3-6): p. 119-123.

65. Cubillas, P., J.T. Gebbie, S.M. Stevens, N. Blake, A. Umemura, O. Terasaki, and M.W. Anderson, *Atomic Force Microscopy and High Resolution Scanning Electron Microscopy Investigation of Zeolite A Crystal Growth. Part 2: In Presence of Organic Additives.* J. Phys. Chem. C, 2014. **118**(40): p. 23092-23099.

66. Kosanović, C., T.A. Jelić, J. Bronić, D. Kralj, and B. Subotić, *Chemically controlled particulate properties of zeolites: Towards the face-less particles of zeolite A. Part 1. Influence of the batch molar ratio $[SiO_2/Al_2O_3]_b$ on the size and shape of zeolite A crystals.* Microporous and Mesoporous Mater., 2011. **137**(1-3): p. 72-82.

67. Sathupunya, M., E. Gulari, and S. Wongkasemjit, *Na-A (LTA) zeolite synthesis directly from alumatrane and silatrane by sol-gel microwave techniques.* J. Eur. Ceram. Soc., 2003. **23**(8): p. 1293-1303.

68. Ghobarkar, H., O. Schäf, and P. Knauth, *Zeolite Synthesis by the High-Pressure Hydrothermal Method: Synthesis of Natural 6-Ring Zeolites with Different Void Systems.* Angew. Chem., Int. Ed., 2001. **40**(20): p. 3831-3833.

69. Jin, N., C. Meng, and J. Hou, *Preparation and characterization of merlinoite for potassium extraction from seawater.* J. Ind. Eng. Chem. (Washington, D. C.), 2014. **20**(4): p. 1227-1230.

70. Ghobarkar, H. and O. Schäf, *Effect of temperature on hydrothermal synthesis of analcime and viséite.* Mater. Sci. Eng., B, 1999. **60**(3): p. 163-167.

71. Qin, Z., L. Lakiss, J.-P. Gilson, K. Thomas, J.-M. Goupil, C. Fernandez, and V. Valtchev, *Chemical equilibrium controlled etching of MFI-Type zeolite and its influence on zeolite structure, acidity, and catalytic activity.* Chem. Mater., 2013. **25**(14): p. 2759-2766.

72. Ghobarkar, H. and O. Schäf, *Synthesis of gismondine-type zeolites by the hydrothermal method.* Mater. Res. Bull., 1999. **34**(4): p. 517-525.

73. Ghobarkar, H., O. Schäf, Y. Massiani, and P. Knauth, *The Zeolite Minerals*, in *The Reconstruction of Natural Zeolites*. 2003, Springer US: Boston, MA. p. 42-124.

74. Ghobarkar, H. and O. Schäf, *Hydrothermal synthesis of laumontite, a zeolite.* Microporous and Mesoporous Mater., 1998. **23**(1-2): p. 55-60.

75. Roth, W.J., P. Nachtigall, R.E. Morris, and J. Cejka, *Two-dimensional zeolites: current status and perspectives.* Chem. Rev. (Washington, DC, U. S.), 2014. **114**(9): p. 4807-4837.

76. Zeng, G., C. Chen, D. Li, B. Hou, and Y. Sun, *Exposure of (001) planes and (011) planes in MFI zeolite.* CrystEngComm, 2013. **15**(18): p. 3521-3524.

77. Holden, M.A., P. Cubillas, M.P. Attfield, J.T. Gebbie, and M.W. Anderson, *Growth mechanism of microporous zincophosphate sodalite revealed by in situ atomic force microscopy.* J. Am. Chem. Soc., 2012. **134**(31): p. 13066-13073.

Graphic Table of Contents (TOC)

Zeolite Surfaces

152,992 Slabs of Arbitrary Thickness

651,850 Slabs of Set Thickness

16.6 Å

405 Wulff Constructions

ANA Predicted Shape

IZA Database